

Texture of average solar photospheric flows and the donut-like pattern

T. Roudier¹, J. Ballot¹, J.M. Malherbe², and M. Chane-Yook³

¹ Institut de Recherche en Astrophysique et Planétologie (IRAP), Université de Toulouse, CNRS, UPS, CNES, 14 avenue Edouard Belin, 31400 Toulouse, France

² Observatoire de Paris, LESIA, 5 place Janssen, 92195 Meudon, France, PSL Research University, CNRS, Sorbonne Universités, UPMC Univ. Paris 06, Univ. Paris Diderot, Sorbonne Paris Cité

³ Institut d'Astrophysique Spatiale, CNRS, Université Paris-Saclay, 91405 Orsay, France

Received march , 2022; Accepted xxx

ABSTRACT

Context. Detailed knowledge of surface dynamics is one of the key points in understanding magnetic solar activity. The motions of the solar surface, to which we have direct access via the observations, tell us about the interaction between the emerging magnetic field and the turbulent fields.

Aims. The flows computed with the coherent structure tracking (CST) technique on the whole surface of the Sun allow for the texture of the velocity modulus to be analyzed and for one to locate the largest horizontal flows and determine their organization.

Methods. The velocity modulus maps show structures more or less circular and closed which are visible at all latitudes; here they are referred to as donuts. They reflect the most active convective cells associated with supergranulation. These annular flows are not necessarily joined as would seem to indicate the divergence maps.

Results. The donuts have identical properties (amplitude, shape, inclination, etc.) regardless of their position on the Sun. The average donuts computed from all the donuts shows an asymmetry east-west of the amplitude which is related to previous works on the wave-like properties of supergranulation. A kinematic simulation of the donuts' outflow applied to passive scalar (corks) indicates the preponderant action of the selected donuts which are, from our analysis, one of the major actors for the magnetic field diffusion on the quiet Sun.

Conclusions. The absence of donuts in the magnetized areas (plages) indicates the action of the magnetic field on the strongest supergranular flows and thus modifies the diffusion of the magnetic field in that location. The detection of the donuts is a way to locate – in the quiet Sun – the vortex and the link with the jet, blinkers, coronal bright points (campfires), or other physical structures. Likewise, the study of the influence of donuts on the evolution of active events, such as the destruction of sunspots, filament eruptions, and their influences on upper layers via spicules and jets, could be done more efficiently via the detection of that structures.

Key words. Sun: supergranulation – Sun: activity

1. Introduction

Dynamics of the solar photosphere has a direct impact on solar magnetism and the evolution of higher layers of the atmosphere, that is, chromosphere and corona. More specifically, the supergranular-scale flows on the solar surface contribute to the solar cycle by diffusing the magnetic flux in the quiet Sun and eroding active regions. Understanding the organization and the physical properties of motions at the solar surface is thus essential to constrain these processes. Different dynamical scales are observed in the kinetic energy spectrum at the surface of the Sun, with the two main scales being the granulation (~ 1 Mm) and the supergranulation (~ 30 Mm). The physical nature of the latter is still elusive and needs to be better understood. Different approaches can be used to determine the properties of supergranulation: it can be seen either by directly following the dynamics of the photosphere thanks to Dopplergrams or reconstructions of horizontal flows, (local) helioseismology (Duvall & Gizon 2000; Berrilli et al. 2004; Hirzberger et al. 2008; Langfellner et al. 2015b), or the organization of the magnetic field or its

absence (voids), for example (Orozco Suárez et al. 2012; Berrilli et al. 2014).

The lattice of the bright emission network visible in the Ca II K line (Simon & Leighton 1964) is located at the edge of the supergranules, and thus it is also a way to characterize the supergranulation. However, this approach may be biased by the way the network is drawn automatically (e.g., tessellation of the Ca II network or segmentation of the divergence field or watershed basin lines (Srikanth et al. 2000; DeRosa & Toomre 2004; Del Moro et al. 2004; Goldbaum et al. 2009)) or manually. It can be subject to the law of closure (also known as the Gestalt laws of grouping), which states that breaks in an object are not perceived and that the object is viewed as continuous, in a smooth pattern. So, Ca II patterns (or other proxies, such as the magnetic field, or UV AIA 1660 or 1700 Å) in some cells are well defined but many are not and they can be detected automatically by eye or using algorithms without being sure of their validity.

In Dopplergrams, it is difficult to find matching pairs of blue- and red-shifted features that define supergranules all over the solar surface, especially at the disk center (Cliver & Knipp 2021). Computing spatial spectra of flows is a common approach to identify the most energetic spatial scales of the pho-

Send offprint requests to: T. Roudier,
e-mail: thierry.roudier@irap.omp.eu

tosphere. However, this method does not allow us to obtain detailed morphological and temporal properties of supergranules (Getling & Kosovichev 2022). In the same way, the works by Švanda (2013); Langfellner et al. (2015a, 2016, 2018) used average supergranules to extract general properties, but this suppressed information on their localization and concealed their diversity in shape, size, amplitude, or orientation. The supergranulation properties are nevertheless relatively sensitive to the technique used. Thus the measurement of the characteristics of supergranules (shapes, sizes, lifetimes, evolution, and downflows) is a challenge, especially in the disk center.

Supergranules associated with the horizontally moving material, with a divergence structure signature, are generally described as being distributed roughly uniformly over the entire solar surface. More specifically, supergranulation characterized by radial flows is often assimilated as jointed cells of various sizes and shapes. It has been noticed that observed properties could depend on the instrument used to quantify the supergranulation flows, with some consequences on the physical descriptions of supergranulation (Williams et al. 2014). The heterogeneity of flows in terms of size and amplitude is well visible in Fig. 1 of Rieutord et al. (2008). This large field of view, at the disk center, not only reveals zones with large amplitude diverging flows, which are not necessarily adjacent, but also shows large regions with low amplitude velocity with low or not diverging vectors.

So we proposed to develop a different approach that minimizes various flaws of previously cited methods. Our method help us to describe the texture of the velocity field at the solar surface. The texture analysis returns information on the spatial arrangement of intensities, in all or parts of the image. Here, the texture of the velocity modulus reflects a general appearance with certain parts having a signature arrangement (circle, disk).

The CST (Roudier et al. 2012; Švanda et al. 2013; Roudier et al. 2013; Rincon et al. 2017; Roudier et al. 2018b) allowed us to follow the horizontal velocities on the whole surface of the Sun with very high spatial (2.5 Mm) and temporal resolution (30 minutes). The CST is a set of codes written in IDL and Fortran 90, computing the horizontal velocity field on the Sun surface by using solar granules as a tracer. With this technique, we can describe the structure of surface velocities in detail and locate, for example, the largest horizontal flows and analyze how they are organized (cells, waves, etc.). We can then verify if these structures are or are not linked to strong positive divergences. Our main goal is to identify the regions where the supergranulation is the most effective and to determine if it can be related to other physical structures, such as vortexes, jets, blinkers, or coronal bright points (campfires). The diffusion of the magnetic flux tubes by the supergranule flows is studied through the evolution of corks, that is, passive scalars.

For the present study, we took advantage of the long-term observations of Helioseismic and Magnetic Imager (HMI) instrument onboard the Solar Dynamics Observatory (SDO) spacecraft and we applied our new approach based on the CST. We investigated the modulus of the surface velocity to describe the texture of photospheric flows. In Sect. 2, we describe the data selection and our reduction pipeline to get the velocity field in spherical coordinates. In Sect. 3, we present the texture of the photospheric flows, and we discuss the detection of the annular structures flows, called donuts, in the velocity modulus field. We describe their properties and characteristics in Sect. 4. The modeling and the evolution of passive scalar (corks) are presented in Sect. 5. Finally, in Sect. 6, we point out a possible link between

the density of donuts and the magnetic field amplitude, before concluding in Sect. 7.

2. HMI data selection and reduction

The HMI instrument aboard the SDO spacecraft (Scherrer et al. 2012; Schou et al. 2012) provides uninterrupted observations over the entire solar disk. The HMI intensity-Dopplergram images observed at wavelengths around the 617.3 nm spectral line of neutral iron Fe I and allow for the photosphere at a 45-second cadence and a pixel of $0.5''$ to be studied. This allowed us to measure the photospheric velocity fields during six consecutive days with uniform observation sets. Using the HMI/SDO white-light data from 26 November to 1 December 2018, we derived horizontal velocity fields from image granulation tracking (Roudier et al. 2012). Two additional sequences were also used for the present study: the first one being on 14 January 2016 to study the supergranulation properties in active areas and the second one being on 28 January 2018 to detect potential links between supergranulation and the eruptive filament.

Different corrections have been applied in alignment, relative to resizement, limbshift correction (Rincon et al. 2017). The differential rotation profile was adjusted from the raw Doppler data averaged over the 24 h of observations. For the derotation procedure, we used a rotation profile that took only large scales into account (supergranules were averaged in space and time):

$$\Omega(\theta) = A + B \sin^2 \theta + C \sin^4 \theta, \quad (1)$$

where $A = 2.864 \times 10^{-6}$, $B = -5.214 \times 10^{-7}$, and $C = -2.891 \times 10^{-7} \text{rad} \cdot \text{s}^{-1}$.

It gives a velocity of 1.9934 km/s (or $14.1781^\circ/\text{day}$) at the equator. Solar differential derotation has been applied on 26 to 28 November from the left to the right (east to west) and on 29 November to 1 december from the right to the left (west to east), since the derotation reference date is 29 November at 00:00 UTC.

The “derotation” of the solar data has been applied to the original data (intensity and Doppler). This consisted in correcting the mean differential rotation of the Sun to bring back longitudes related to the solar surface at the same locations for each time deviation from the origin of the first HMI image. The reference day for the CST code (see manual of the CST codes¹) was taken at 00:00 UTC, 29 November 2018, which is the middle of our sequence. In the same way, for both sequences on 14 January 2016 and 28 January 2018, the time reference of the derotation was taken at 00:00 UTC for each date.

From a CST (Roudier et al. 2012) of photometric structures, such as granules, we derived the projection of the photospheric velocity field (u_x, u_y) onto the plane of the sky/CCD matrix. The u_x and u_y (in km/s) were computed at a cadence of 30 min with a spatial window of seven pixels, equivalent to $3.5''$, that is, around 2.5 Mm. The CST velocities were complemented by HMI Dopplergrams to form full velocity vectors. The pipeline running at Institut de Recherche en Astrophysique & Planétologie (IRAP) resulted in full-disk maps of the zonal, meridional, and radial components of the surface flow with a cadence of 30 min. It has been shown in previous papers (Rincon et al. 2017; Roudier et al. 2018b, 2012) that the CST allows the study of both small ($> 2.5\text{Mm}$) and large velocity scales at the solar surface.

¹ https://idoc.ias.u-psud.fr/system/files/user_guide_annex_version1.2_26mars2021.pdf

The combination of the results with Doppler data, which provides the out-of-plane component u_z of the velocity field, allowed us to calculate the full vector velocity field at the surface in solar spherical coordinates u_r , u_θ , and u_ϕ , where θ and ϕ denote the latitude and the longitude, respectively. We computed the 30-min-averaged horizontal surface velocity field $\mathbf{u}_h \equiv (u_\theta, u_\phi)$ (Roudier et al. 2018b). We obtained 288 velocity maps spanning over the six days of observation (26 November to 1 December 2018). The velocity modulus is $u_h = |\mathbf{u}_h| = \sqrt{u_\theta^2 + u_\phi^2}$.

3. Structure of horizontal flows

3.1. Photospheric horizontal flows' texture

A smoothing window of 12h was applied during the entire 6-day sequence to reduce the velocity noise and to study the texture, in a topological context, of the photospheric horizontal flows \mathbf{u}_h at the supergranulation timescale. The velocity modulus u_h and horizontal divergence $\nabla \cdot \mathbf{u}_h$ were derived for every single snapshot of the 30-min horizontal velocity. An example horizontal divergence and the velocity modulus averaged over 12 hr from 29 November 2018 are plotted in Fig. 1. The temporal evolution of the derotated horizontal velocity modulus and divergence fields during 6 days can be watched in movies 1 and 2 (Fig. A.1, Fig. A.2), respectively. A combination of movies 1 and 2 is given in movie 3 (Fig. A.3).

The divergence field shows positive structures (white) in Fig. 1 (top), with a paving aspect over the entire solar surface, with different sizes and amplitudes. The maximum amplitude of that divergence structures was found to be $9 \cdot 10^{-5} \text{ s}^{-1}$ and the mean size corresponds to the supergranule one (about 20 Mm). However, a region with positive divergence does not necessarily correspond to an isotropic structure in the underlying velocity field. Indeed, we observed that large amplitudes of the divergence can also be produced by a velocity gradient in a privileged direction.

The velocity modulus u_h , in Fig. 1 (bottom), reveals another texture of the flow where the spatial organization of the pavement is less visible and is less distributed homogeneously with large areas of lower amplitude. This kind of donut is also visible (see Fig. 2) in a previous observation at a higher spatial resolution obtained with the Hinode/SOT instrument (Roudier et al. 2009) from 29 to 31 August 2007. Figure 2 shows a clear donut that is visible in the horizontal velocity modulus. Its amplitude is greater than the one of its neighborhood. The larger amplitude of velocity is located close to the edge of the tree of fragmenting granules (TFGs). The top and bottom images of Fig. 2 show the effect of the temporal averaging, which increases the isotropic aspect of the donuts. One possible scenario of donuts' creation is due to the horizontal velocities' evolution related to the TFGs (Roudier et al. 2016). These coherent flows tend to form the isotropic flows (donuts) from the development of spatially close and temporally, almost simultaneous, TFGs (Roudier et al. 2016). The other locations with large divergences, but weak unstructured u_h , are probably generated by isolated TFGs, with a lower velocity amplitude and none being in phase with their neighbors. The most striking patterns in this map are the almost circular and closed structures visible at all the latitudes. These structures, with an annular-shaped flow that formed by the 12h average of the horizontal velocity magnitude, certainly reflects the most active convective cells associated with supergranulation. These annular-shaped flows are also visible with a 2h average, but they are noisier. This irregular diffuse rings have been

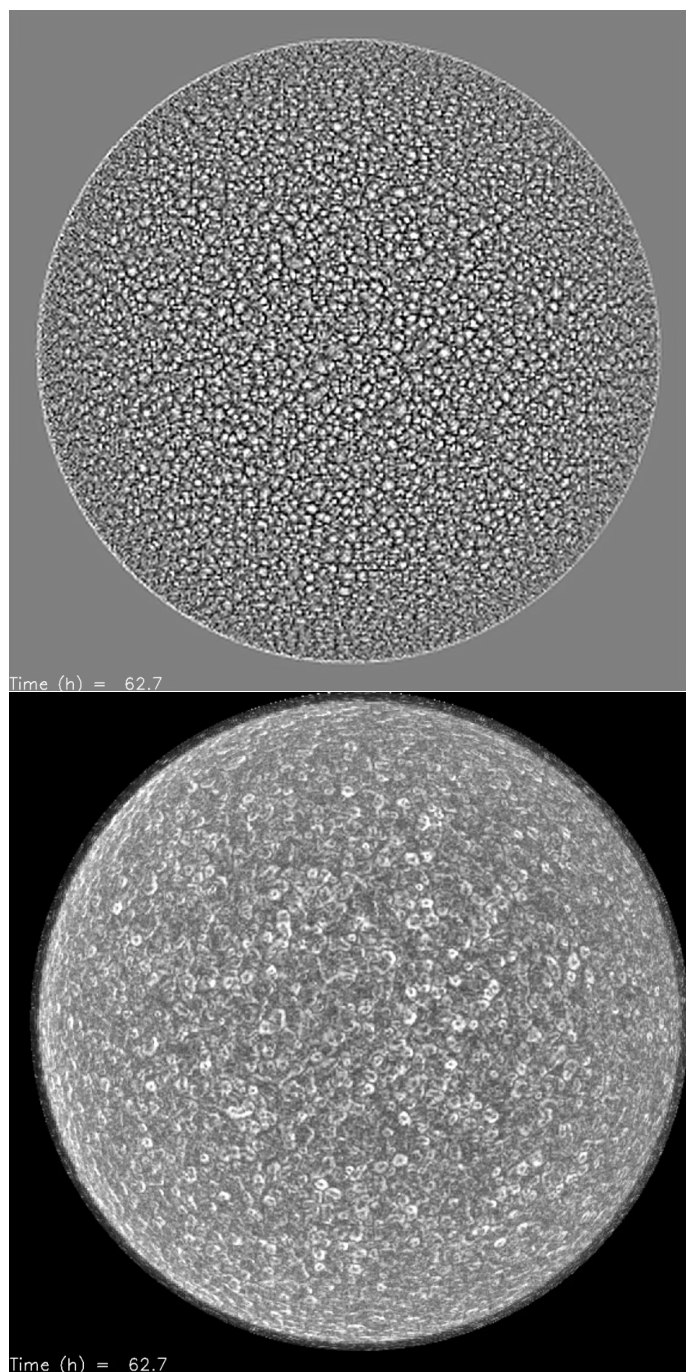


Fig. 1. top) Divergence and (bottom) modulus maps of the horizontal velocity \mathbf{u}_h , averaged over 12 hrs, on 29 November 2018.

observed previously by Shine et al. (1999). For convenience, we referred to these annular structures as “donuts” in that paper (and not in solar physics in general) because these elements represent only a characteristic of the motions of the surface at the scale of the supergranulation. The present works are mainly focused on the characterization of these elements.

On the full Sun velocity modulus map, large areas without a donut are visible. In these regions, the amplitude of the flows are weak and they are not clearly structured.

This kind of donut is also visible (see Fig. 2) in a previous observation at a higher spatial resolution obtained with the Hinode/SOT instrument (Roudier et al. 2009) from 29 to 31 August 2007. Figure 2 shows a clear donut that is visible in the hori-

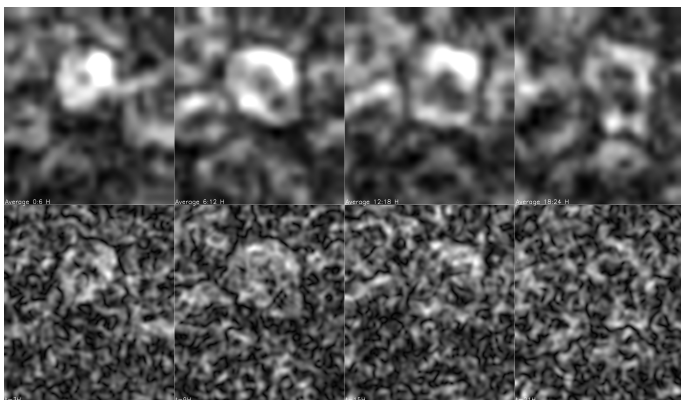


Fig. 2. Top row shows the evolution of the horizontal flow modulus observed by Hinode from 29 August 2007, 10:17 UT to 31 August 2007, 10:19 UT, with a spatial resolution degraded to the one HMI/SDO. In each frame, the flow modulus is averaged over 6 hrs. Each frame is separated by a time step $\delta t = 6$ h. The bottom images represent the 30-min averaged horizontal flow modulus corresponding to the middle time of each averaged top modulus maps. Fields of view span $90'' \times 93''$ (62.25×67.43 Mm²).

zonal velocity modulus. Its amplitude is greater than the one of its neighborhood. The larger amplitude of velocity is located close to the edge of the tree of fragmenting granules (TFGs). The top and bottom images of Fig. 2 show the effect of the temporal averaging, which increases the isotropic aspect of the donuts. One possible scenario of donuts' creation is due to the horizontal velocities' evolution related to the TFGs (Roudier et al. 2016). These coherent flows tend to form the isotropic flows (donuts) from the development of spatially close and temporally, almost simultaneous, TFGs (Roudier et al. 2016). The other locations with large divergences, but weak unstructured u_h , are probably generated by isolated TFGs, with a lower velocity amplitude and none being in phase with their neighbors.

3.2. Donut identification

We aim to characterize the donuts in terms of locations, sizes, amplitudes, lifetimes, and shapes. At the beginning of this study, different techniques to isolate the donuts automatically were performed, such as watershed segmentation, neural networks' processing, among others. However, the results of these various approaches did not allow us – in our special case of donut selection – to isolate, exhaustively with confidence, all the visually detected donuts. This is especially due to the low-velocity contrast, the residual noise, and the inhomogeneous intensity repartition in the donuts that were easily identified by eye and brain of observers, and to the small number of structures (110) in the data to educate, for example, a neural network.

Then, to start our study on a greater number of donuts, we decided not to use automatic recognition of the donuts and detected them directly by eye by checking them attentively. In that first step, we concentrated our work on the two central days (28 and 29 November 2018) where the derotation allowed for the full Sun to be covered. This enlarged donut sample was used, in a second step (see chapter 6.1), to detect the donuts as automatically as possible with confidence.

In order to flawlessly detect all the structures with an annular shape, we used a widget to watch the temporal evolution in all locations on the Sun surface. In the present study, we are interested in isolating the largest amplitude and clearly recognizable u_h annular structures. Some low amplitude and not fully closed

structures with a short lifetime are probably lost; however, regarding our goal, we consider that their contributions are small, in particular in the magnetic element diffusion for example.

During that period of two days, 554 donuts were detected on the area located between $\pm 60^\circ$ in latitude and longitude, giving a rate of donuts of 1.05×10^{-9} Mm⁻² s⁻¹. Applying the impact assessment reasoning proposed by Title et al. (1989) for exploding granules to our donut detection, we found, for an average donut area of 353 Mm², an impact of a donut of 747 hrs (i.e., 31 days) for each point on the Sun.

3.3. Donuts' lifetimes and location

To measure their lifetimes, the data from 27 and 30 November 2018 were used to determine their births and deaths times. Due to the solar derotation, the edge of the solar disk was too noisy and only donuts located between $\pm 60^\circ$ in latitude and longitude were studied. The amplitude of the velocity modulus u_h issued from the spherical components u_θ and u_ϕ does not suffer from projection effects; only the shape is affected (circle to ellipse) and it has been taken into account as for area measurements. The donut birth detection is a delicate point, particularly due to our visual procedure; even the donuts grow up with a ring shape from the beginning. We chose to define the birth of the donuts when the central hole appears in the circular shape of the structure. Due to the low spatial resolution of our data, the determination of the date of birth is defined at ± 1 h. The date of death of the donuts was determined when the circular shape is broken. To limit the effect of the temporal window, the donuts' lifetimes were estimated with a temporal window of 2 h. We did not consider the evolution of donut pieces resulting from donut breaking and their possible impact on the surface dynamics. However, we roughly estimated that those pieces typically survive only one or two hours. Thus, regardless of whether this extra time is taken into account, it would not significantly modify the lifetimes ranging between 2 h and 55 h with a maximum of around 24 h (see Fig. 8 top left), with a global incertitude of around 3 h, which is characteristic of the supergranule lifetime (Rincon & Rieutord 2018). Figure 3 shows the temporal evolution, with different temporal windows of two donuts, where the birth (low line of the temporal cut) and death (top line in the temporal cut) times are indicated.

The location on the Sun surface of the 554 donuts visually detected between 28 and 29 November 2018 are superimposed (circle) on the average velocity modulus in Figure 4. It corresponds to a quiet Sun period. We also compare the location of donuts with the magnetic field in Fig. 5. Most of the donuts are located in low amplitude magnetic field regions. A magnetic network is generally organized around the donuts. However, the links between the magnetic field and donuts are subtler than their relative location and this is described below (Sect. 5.3). The location of the donuts to the coronal hole visible in the SDO (193Å) observation on 28 and 29 November 2018 does not reveal any particular spatial distribution of the donuts relatively to the coronal hole ².

4. Donut properties and characteristics

4.1. Donut morphological properties

Once we detected donuts in time (birth to death) and space (latitude and longitude), we measured their shape and intensity dis-

² https://sdo.gsfc.nasa.gov/data/dailymov/movie.php?q=20181128_1024_0193

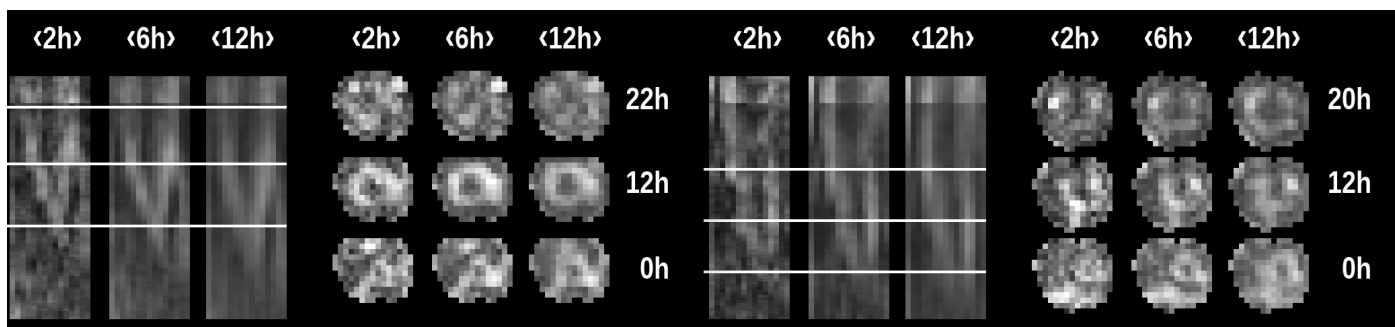


Fig. 3. Two examples of donut evolution from their birth (a central hole appears) to their death (broken structure). Temporal cuts with different temporal averaging windows (2h, 6h, and 12h) in the center of each donut (on the left of each example) are shown. On the right side, for each donut, cuts are shown at different times (0h, 12h, and 22h left donut example) and (0h, 12h, and 20h for the right donut example). These times are overplotted for each donut in their temporal respective cuts. In each case, the birth and death times correspond to the low and top white line of the respective temporal cuts. Plotted fields span $8'' \times 8''$ ($5.8 \times 5.8 \text{ Mm}^2$).

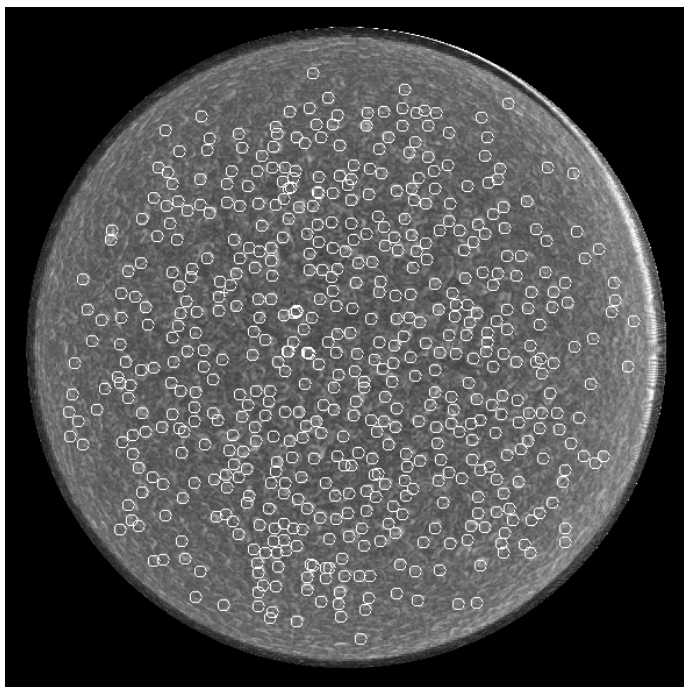


Fig. 4. Circles indicate the 554 detected donuts on a map showing the averaged horizontal velocity u_h on 28-29 November 2018.

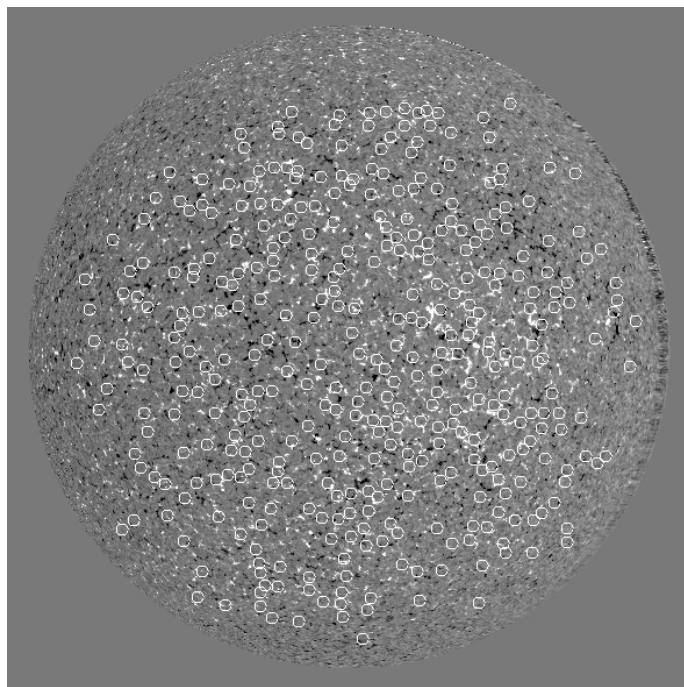


Fig. 5. Location of detected donuts (circles) superimposed on a map of mean longitudinal magnetic field $\langle B_{||} \rangle$ on 29 November 2018, averaged between 12:00 to 24:00 UTC.

tribution. More precisely, to determine the zone of influence of each donut, we averaged u_h over its lifetime, and we applied a watershed technique to segment the mean structure (Roudier et al. 2020). Figure 6 shows some examples of donuts averaged during their lifetime (left column) and their segmented (binarized) counterpart (middle column). To determine their shape, area, and orientation, each averaged donut was fitted with an ellipse (see Fig. 6, right column). In addition, we measured their intensity distribution and evolution during their lifetime.

4.2. Mean donuts at the disk center

First, we computed a mean donut close to the disk center ($\pm 10^\circ$) to avoid projection effects, by averaging all the 36 detected donuts in that area. Figure 7 clearly shows the roundish shape of the “mean donuts” with an estimated radius of 11 Mm and a velocity amplitude, at the donut radius, up to 650 m/s. The modulus velocity in the center of the mean donuts of $404 \pm 78 \text{ m/s}$ reflects

the diversity of the shape, intensity, and centering of all the averaged donuts. At the individual donuts’ center, at the disk center, the velocity is found to be around 157 m/s and is close to the level of the noise. An asymmetry of the velocity amplitude is clearly visible between the east (left) and west (right) sides. We could think that the differential rotation may produce such an asymmetry. However, as mentioned in Sect. 2, we applied a derotation procedure. The observed excess of velocity amplitude on the west side, on the average donuts, is quite probably of a solar origin. This east-west anisotropy can be related to the previous observations showing that asymmetry in intensity (Langfellner et al. 2016), and related to anisotropy in the network where the network magnetic field is stronger in the west (in the prograde direction) than in the east (Langfellner et al. 2015a; Roudier et al. 2016). This east-west anisotropy is related to the wave-like properties of supergranulation. These waves were found to travel predominantly in the east-west direction, with more power in the prograde direction, and this excess in westward power leads

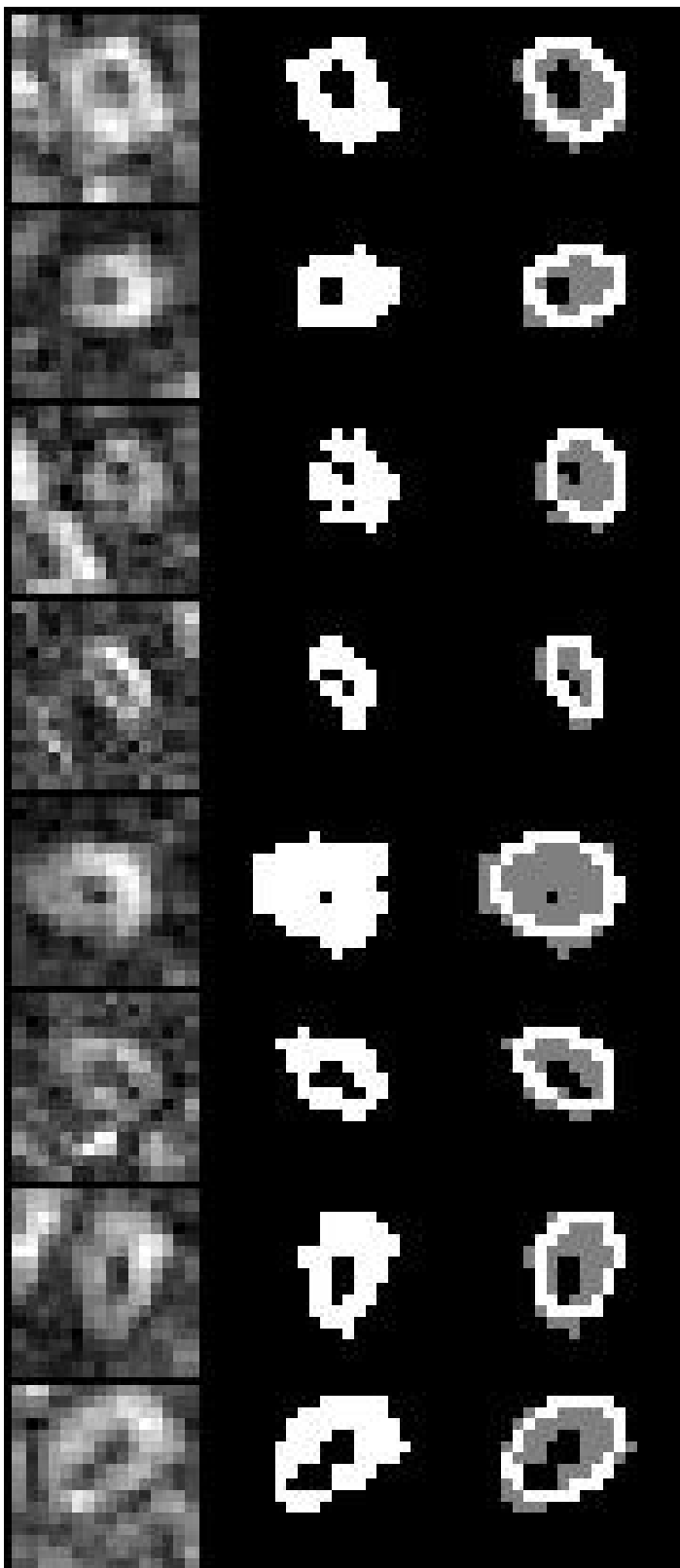


Fig. 6. Examples of donuts' $|u_h|$ velocity modulus (left), segmented (middle) and adjusted with ellipses (right). The field of view is $58.9'' \times 58.9''$ ($42.1 \times 42.1 \text{ Mm}^2$).

to the observed super-rotation of the pattern (Langfeller et al. 2018).

By widening the fields in latitude and longitude, for example by considering a field of $\pm 20^\circ$ with 130 detected donuts, we still

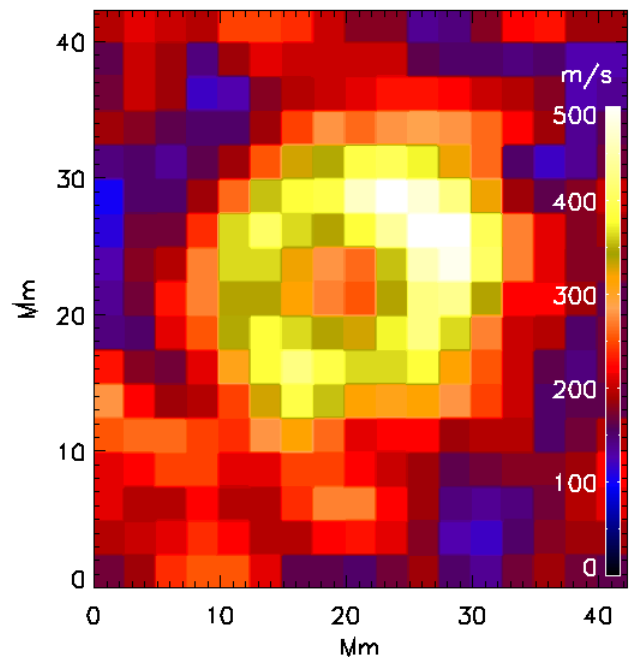


Fig. 7. Mean donuts computed from donuts in latitude and longitude $\pm 10^\circ$ around the disk center. The estimated radius is 11 Mm with a mean modulus velocity at the center of $404 \pm 78 \text{ m/s}$ and of $650 \pm 65 \text{ m/s}$ on the donut corona (white).

observed this asymmetry of the velocity modulus of the mean donut. This suggests that such a property is found up to the whole Sun and not only at the disk center.

4.3. Donut characteristics

One of the advantages of the CST is to get the modulus surface flow u_h at the disk center and then to give the possibility to follow the donuts with a high temporal resolution (2 h). The segmentation of the donuts described above allowed us to determine the parameters that characterize these objects. We measured their area and corrected them for spherical projection effects. Their distribution is shown in Figure 8 (top right). It lies between 80 and 900 Mm^2 and peaks around 350 Mm^2 ; this is equivalent to a radius of 10.6 Mm, which corresponds to the typical supergranule size. Surprisingly, no clear correlation has been found between the lifetime and the area: some small donuts have a long lifetime, whereas some large ones have short lives.

In the same way, we did not find any correlation between the different parameters, such as the donuts corrected area, tilt angle, or the isotropy of the donuts, and their location on the solar surface. This seems to indicate a relative homogeneity of the donut geometrical properties all over the solar surface.

The mean velocity modulus was extracted for each donut from its location and segmented area. The mean velocity distribution peaks at 0.48 km/s (Fig. 8 bottom left); this does indeed correspond to the mean supergranular horizontal velocity amplitude (Rincon et al. 2017). The amplitude lies between 0.35 and 0.63 km/s. No correlation has been found between the mean velocity modulus and the donuts areas, and also latitude, confirming our previous remarks about the homogeneity of donut properties over the solar surface. We compared the distribution of u_h inside the donuts to its distribution in the full field at the disk center (in a field of $\pm 20^\circ$ in latitude and longitude), on 29 November

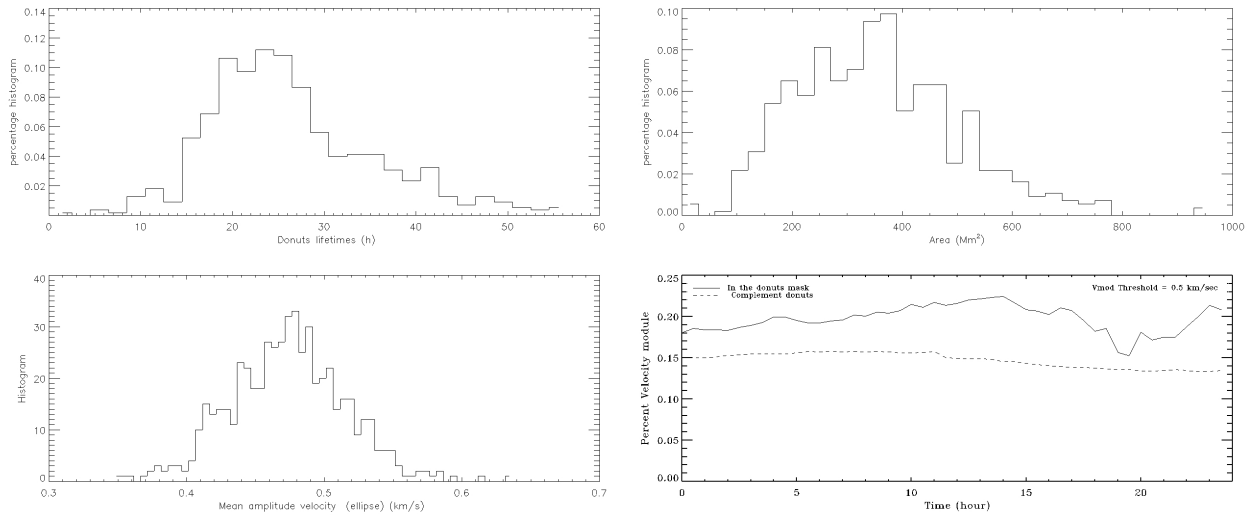


Fig. 8. Top: Distribution of donut lifetimes (left) and distribution of donut areas corrected for projection effects (right). Bottom: Distribution of mean velocities inside donuts (left) and percentage of the area with a velocity greater than 0.5 km/s in donuts (solid line) and in the complementary field (dashed line) at the disk center $\pm 20^\circ$ in latitude and longitude (right). These distributions come from data from 29 November 2018.

2018. Values inside the donuts are significantly higher regardless of the temporal window used (see Table 1). This indicates that the detected donuts are the most important patterns in terms of horizontal flows on the Sun surface. This property is confirmed by the time evolution of the percentage of area occupied by the velocity modulus higher than 0.5 km/s on the same field and in the donuts (Fig. 8 bottom right).

Table 1. Mean velocity inside and outside donuts above different velocity thresholds (0.5, 0.8, 1.0 km/s) at the location of $\pm 20^\circ$ in latitude and longitude. The left column gives the temporal window used, the central column corresponds to the mean velocity inside the donuts, and the right column is the mean velocity outside the donuts

temporal window	mean velocity inside (km/s)	mean velocity outside (km/s)
only above 0.5 km/s		
2h	0.641	0.611
6h	0.626	0.590
12h	0.619	0.571
only above 0.8 km/s		
2h.	0.977	0.868
6h	0.970	0.842
12h	0.958	0.841
only above 1.0 km/s		
2h	1.196	1.040
6h	1.153	1.152
12h	1.147	1.033

We also explored the difference between the amplitude of the divergence inside and outside the donuts. We show their distributions in Fig. 9. Comparing both histograms reveals that the divergence has a larger amplitude inside the donuts. Thus, the donuts represent the most powerful divergent events on the solar surface.

5. Impact of donut evolution on surface diffusion

From our previous analysis, the donuts reflect the most active convective cells associated with supergranulation. So it appears

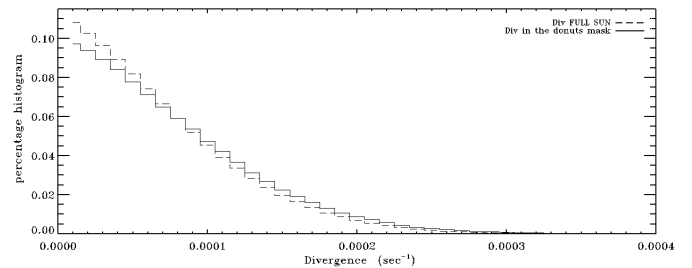


Fig. 9. Distribution of divergence amplitude in donuts (solid line) and in the full Sun (dashed line).

natural to measure the influence of these photospheric motions, linked to donuts, on the evolution of solar magnetism and activity. The transport of those magnetic elements in the photosphere and understanding the mechanism that diffuses magnetic fields is still a challenge. Using the proxy of magnetic elements, we can follow the evolution of an initially randomly distributed passive scalar (corks) to characterize the transport properties of the turbulent velocity field of the solar surface.

5.1. Donut modeling

We aim to determine the influence of donuts on the evolution of the photospheric magnetic field on the solar surface. To avoid the other components of the velocity field (solar rotation, meridian circulation, etc.) and to isolate the role of donuts, we built the velocity field generated by only the simulated radial outflows of the donuts.

To simulate the horizontal flows generated by donuts, we used a simple kinematic description, previously used by Simon & Weiss (1989); Simon et al. (1991). Thus, we modeled the horizontal velocity inside a donut as a divergent flow around its center with a modulus

$$u_h(r) = u_0 \frac{r}{R} \exp\left[-\frac{1}{2}\left(\frac{r}{R}\right)^2\right], \quad (2)$$

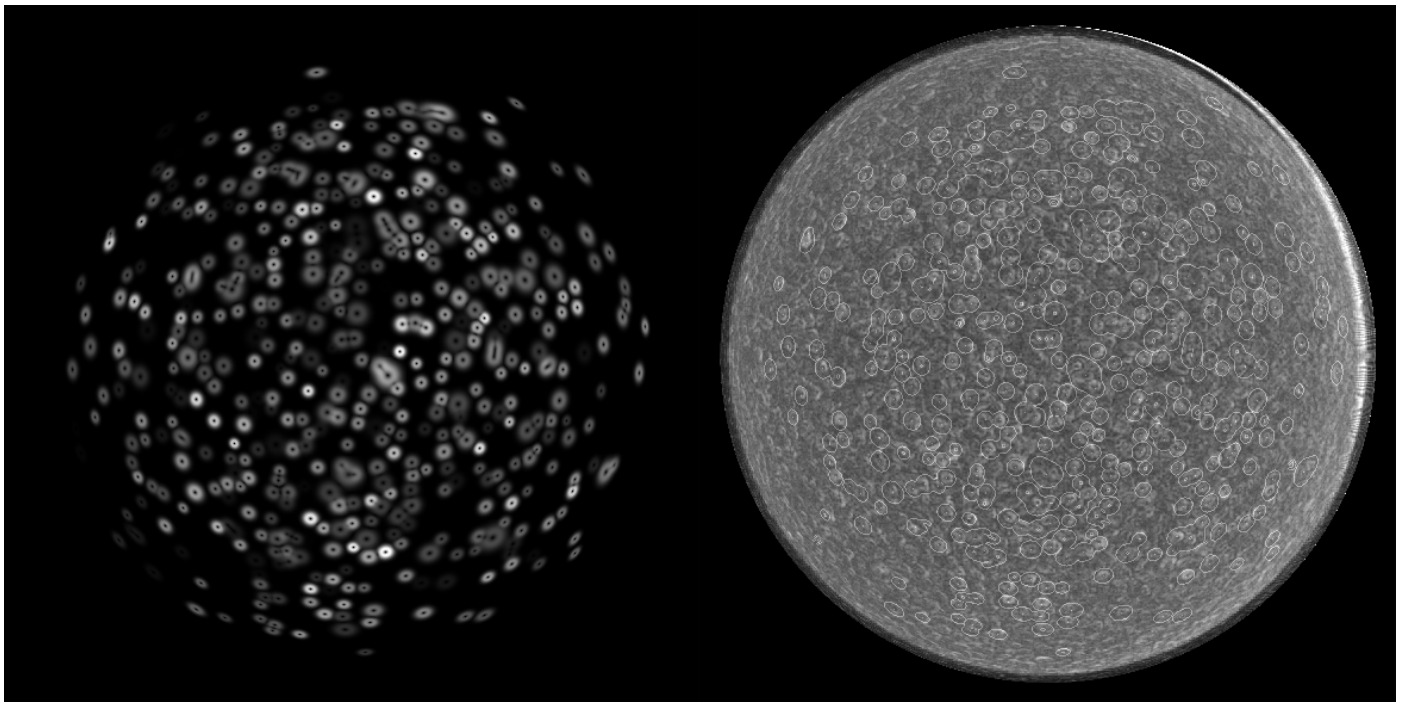


Fig. 10. Left: Map of u_h of simulated donuts averaged on 28-29 November 2018, taking into account their locations, lifetimes, velocities amplitude, and the projection effects. Right: Observed velocity modulus u_h averaged over 28-29 November 2018 and contour of the simulated donuts overlapped on the same period.

where r is the distance to the center, R the radius of the donut, and u_0 the amplitude of the field velocity. This profile was obtained by assuming that the source of the horizontal flow follows a Gaussian distribution.

We note that this function is purely qualitative; the divergence of u_h is zero for $r = R$, positive for $r < R$, and negative for $r > R$. It assumes circular symmetry, which is a first approximation. Such a spatial isotropic function was used to model each of the 554 donuts, as well as the 3D files taking into account how the spatial and temporal location of them is built. The temporal average of this simulation is illustrated in Fig. 10 (left) and can be compared to the averaged velocity modulus on 28–29 November 2018 in Fig. 10 (right). To get a more realistic modeling of the donut outflow in function of their location on the solar surface, we took into account the projection effects with the center-to-limb angle. Some donuts were not included in the simulation because they were born just before the end of the 2 days and they have been excluded. In the velocity histogram of all the simulated donuts' flows, most of the velocity modulus lies between 0 and 400 m/s, which is perfectly representative of the amplitude supergranulation horizontal flows.

5.2. Evolution of corks on the solar surface

To mimic the behavior of the magnetic flux tubes' evolution on the solar surface, (Simon et al. 1991) we used passive test particles (also called corks) whose trajectories are guided by the flow created by the donuts. The flow displaces the corks from their initially uniform grid distribution. The development of cork patterns in the field, over the two days, evolved from the uniform distribution over the surface to a structured shape. Figure 11 shows the final positions of all the corks relative to the averaged longitudinal magnetic field between 12:00 and 24:00 on 29 November 2018. The fraction of the area devoid of corks was estimated at 65% in the disk center (to avoid projection effects).

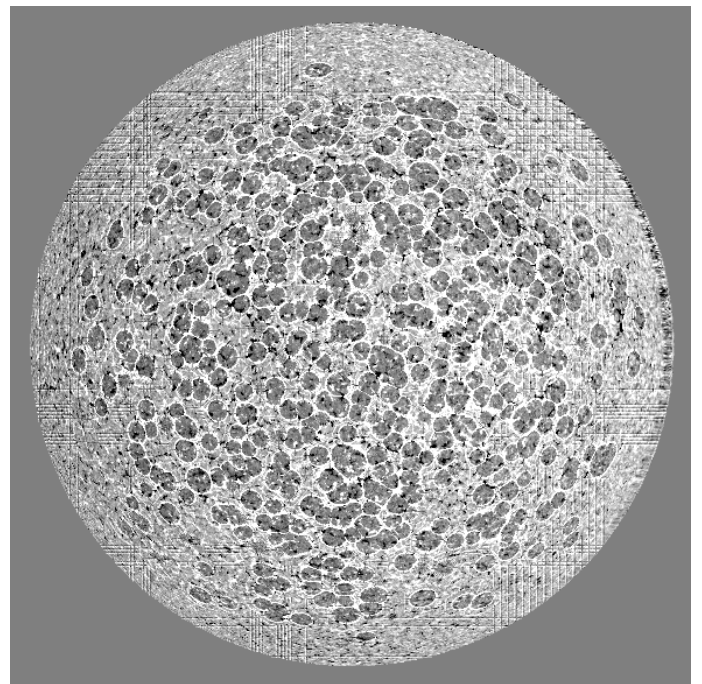


Fig. 11. Final positions of the corks after two days of evolution overlapped on the mean magnetic longitudinal field $\langle B_{||} \rangle$ on 29 November 2018, from 12:00 to 24:00.

The network created by the diffusion of these corks is not exactly superimposed on the magnetic network of the quiet Sun, but it shows a large number of magnetic empty regions of these free zones of corks. This seems to us to be a consequence of the selection of axisymmetric structures (donuts) that we have carried out, losing the other surface motions that do not fit in the donut category. Nevertheless, we see the influence of the only

selected structures (donuts) which have a preponderant action in the diffusion of the magnetic field in the quiet Sun. The selected donuts are one of the major actors in the magnetic field diffusion on the quiet Sun. This suggests that the distribution of the magnetic field on the solar surface depends on the most energetic donuts to form the photospheric network or magnetic patches. Small donuts, which do not take our selection into account, seem to play a minor role in the network building.

We took advantage of the multiwavelength observations to compare the positions of the donuts detected on 29 November 2018, with the solar corona observations being made on the same day. Where coronal holes are present, we observe that the regions are emptied of their corks, but it is not clear whether this is statistically significant when compared to the far regions on the solar surface. No formal conclusion can be drawn as to the influence of the donuts' surface distribution and the coronal hole from our sequence.

5.3. Regions with a low velocity modulus

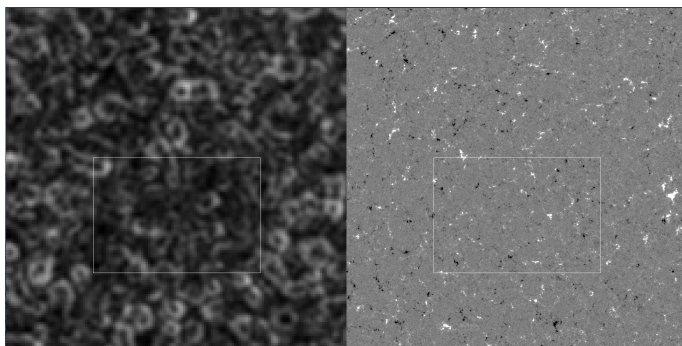


Fig. 12. Low velocity modulus region is in the white rectangle (field of view: $257'' \times 180''$ ($184 \times 120 Mm^2$)) as well as the corresponding longitudinal magnetic field ($B//$).

A closer inspection of the texture of the velocity modulus map allowed us to locate regions where donuts are almost absent or, at best, have low amplitudes compared to the rest of the solar surface. The longitudinal magnetic flux of such a region is shown in Fig. 12. The comparison of the histograms of the absolute value of magnetic flux inside the lower velocity amplitude region (in the white rectangle) and the rest of the magnetic flux is plotted in Fig. 13. A comparison of the histograms reveals a slightly higher magnetic flux amplitude in the lower velocity modulus region, which is in agreement with the action of the magnetic field on the turbulent motions. However, the difference is small and we observed, in our data, only a few cases; this will have to be confirmed with a more statistical analysis.

6. Possible link between donuts and dynamical events of the solar outer solar atmosphere

The potential action of the photospheric motions linked to donuts onto the dynamics of the outer solar atmosphere, such as the triggering of filament eruptions or many other applications on phenomena where surface motions are involved, is particularly interesting to contemplate. The solar atmosphere, from the photosphere to the chromosphere and toward the corona, is not static.

In the photosphere, the magnetic field is subject to diffusion due to supergranular flows and the large-scale motions of differential rotation and meridional circulation (Fan 2021). The mag-

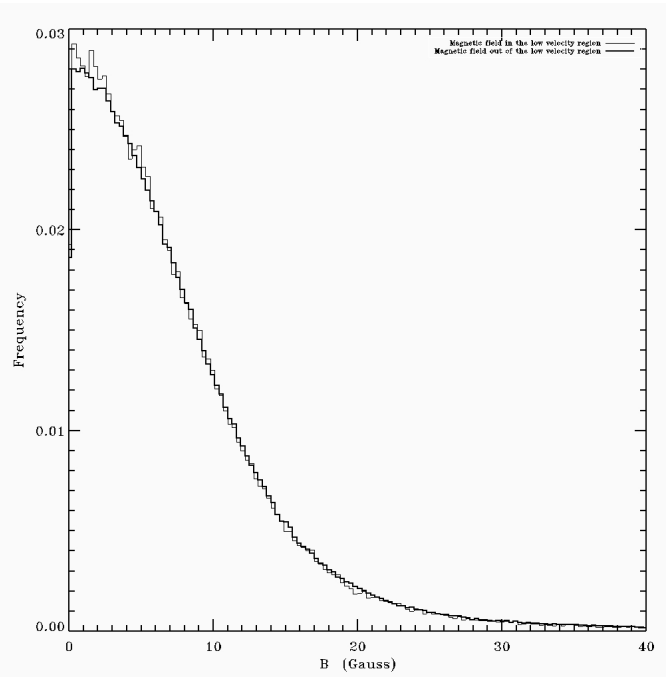


Fig. 13. Histograms of the absolute value of the magnetic flux in and out of the low velocity modulus region. The comparison of the histograms shows a slightly higher magnetic flux amplitude in the lower velocity modulus region.

netic field elements, which are transported across the solar surface by the surface motions, cause shearing of the chromospheric and coronal magnetic field. The dynamics of the photospheric plasma has consequences on the properties of the chromosphere and the corona, in particular via the magnetic field whose elements propagate the disturbances related to the turbulence motion of the solar surface. The strong coupling between convection and magnetic field in the photosphere has a consequence on the magnetic structures at higher solar atmospheric layers. For example, the convection cells transport the magnetic field and form a magnetic polarity inversion line between them (Roudier et al. 2018a). A previous study shows the importance of the photospheric flows for influencing the stability of the structures of the magnetic field in upper layers of the solar atmosphere (Wollmann et al. 2020), for example in the destabilization and eruption of solar filaments.

Other examples are described in the literature such as the coronal plumes which are linked to photospheric flows. The bright plumes form where converging supergranular flows bring unipolar network elements together to form large, dense clumps (Wang et al. 2016). The plume emission fades when the flows diverge again and the clumps are dispersed (Wang et al. 2016).

The long temporal space-borne sequences' observations allow us to show the existence of long, persistent downflows together with the magnetic field. They penetrate inside the Sun but are also connected with the anchoring of coronal loops in the photosphere, indicating a link between downflows and coronal activity. A link suggests that EUV cyclones over the quiet Sun could be an effective way to heat the corona (Roudier et al. 2021).

6.1. Detection of donuts using properties of the divergence field

Different physical dynamical phenomena are observed on the Sun atmosphere, such as a vortex, a jet, blinkers, coronal bright points (campfires), filaments' eruption, sunspot destruction, among others. All of these phenomena occur in a temporal range from a few hours to several days and a spatial range from the solar granulation (1000 km) to scales of several megameters. As the donuts represent an intermediate scale of the described surface phenomena, we found it very interesting to explore potential links between these phenomena and donuts' evolutions. Such studies require a more automatic and rapid detection of donuts. For this purpose, we developed a divergence detection method, described below, and we applied it to the new HMI/SDO sequences: on 14 April 2016 containing plage regions, and on 26 January 2018 including an erupting filament.

The detection of donuts by eye is limited since it is time-consuming and tedious. Nevertheless, this manual donut detection, described above, provided a sufficient sample (554 donuts) to serve as a reference to implement new donut-detection methods as automatically as possible. From the analysis of the 554 donuts, the donuts are found to represent the most powerful divergent events on the solar surface related to supergranulation. So, it was natural to use the divergence field to automate the donut detection to get more detailed and statistical knowledge of their properties (shapes, amplitude distribution, etc.). Even if this method is incomplete, it must at least allow us to detect the largest donuts in shape and amplitude with a good confidence level. The best method, we found, is to use the divergence field calculated by the CST averaged over a few hours (12h or 24h). The best method found is to apply a threshold to the divergence field and keep only the divergence with an amplitude above the selected threshold. This gives a separated area, allowing for the largest amplitude divergence in the field to be located. The center of gravity of these area elements allowed us to detect the potential donut location.

The divergence threshold of $7.2 \times 10^{-5} \text{ s}^{-1}$ allowed us to detect 95% of donuts at the latitude and longitude $\pm 20^\circ$ with a great confidence. Out of a total of 104 donuts detected visually, 99 donuts over 24h were well detected giving a detection error around 5%. Considering the different amplitudes, shapes which are more or less closed, and the proximity of the donuts, that error is acceptable in a lot of studies such as those presented below. The donut rate found is $1.7 \times 10^{-9} \text{ Mm}^{-2} \text{ s}^{-1}$, which is close to those found for a larger field of view ($1.05 \times 10^{-9} \text{ Mm}^{-2} \text{ s}^{-1}$) at the latitude and longitude of $\pm 60^\circ$ with the manual method.

6.2. Donuts and plage regions

The divergence detection method described in the previous section was applied to a new data set on 14 April 2016 and the results are shown in Fig. 14. The donuts are fairly evenly distributed on the solar surface, except in the magnetic regions (plages and sunspots). In particular, no donuts were detected in the plage region. The divergence is less structured and shows low amplitudes in plages and active regions in the north of the Sun. At the same location, we also observed a lower amplitude of the velocity modulus and almost no donut. In the other western region with high amplitude magnetic fields, we also observed a lower velocity modulus and donuts are less present. This clearly indicates that the large magnetic field affects the supergranulation flows and, in particular, those with an axisymmetric shape, which are the most powerful supergranules. It has already been

established that in plage regions, which have higher magnetic fields than quiet regions, horizontal flows are weaker by a factor of two (Title et al. 1992). We also know that supergranulation is affected by the variation of the magnetic field. Our observation is compatible with the results found by Meunier & Roudier (2007), where a high level of weak fields may prevent the formation of large cells. Supergranules are smaller, on average, at cycle maximum than at cycle minimum (Meunier et al. 2008). From our direct observations, we conclude that, in the magnetized areas, the strongest supergranular flows (donuts) are affected and thus also modify the diffusion of the magnetic field in these places.

6.3. Donuts and filament eruptions

From another observation of active area (on 26 January 2016 Roudier et al. 2018a), we confirm the effects of the magnetic field on the formation of donuts (Fig. 15). As described by Roudier et al. (2018a), in the neutral line (southwest) where a filament is located, we observed weaker horizontal velocities, as well as the formation of donuts. Before the filament eruption, we noted horizontal flow activity and intense donuts close to the location of one foot where the eruption started (close to the point C in Fig. 5 of Roudier et al. (2018a)). This point, indicated by the arrow in Fig. 16, is located close to large donuts before the eruption which could be one of the actors of the eruption triggering (Fig. 16, middle and right). However, it would be hazardous to draw a firm conclusion about the relation between filament destabilization and intense horizontal flows produced by donuts from only one observation. A statistical study is needed to clarify the causal relationship between these intense flows and the eruption of the filament.

6.4. Potential link between donuts and the vortex

We now want to locate where the supergranulation is most effective and can be linked to local events. By studying previous publications on supergranules and phenomena close to them (vortices, jets, etc.) described in the literature in detail, we notice that the studied supergranules were well structured, especially with an isotropic distribution of their horizontal velocities as our donuts. We can cite, for example, the first work of Attie et al. (2009), where we can see in their Figs. 3 and 7 the presence of a well-formed supergranule and the presence of a vortex.

Similarly, several analyses of an observation sequence of 2 November 2010 report that the supergranule is well formed: readers can refer to Figure 1 of Giannattasio et al. (2014b), for example, where the horizontal velocity modulus is clearly isotropic as our donuts. This data set (2 November 2010) used in this work was exhaustively described in Gošić et al. (2016), and previously analysed by Giannattasio et al. (2014b,a) and Caroli et al. (2015); Giannattasio et al. (2018). Attie et al. (2016) (Fig. 6 bottom) observed persisting structures such as large-scale vortex flows ($\sim 18 \text{ Mm}$). This is confirmed by Requerey et al. (2018) who, on data from 2-3 November 2010, report a detection of a similar vortex flow at supergranular junctions which consisted of three recurrent vortices (with an amplitude of $1.5 \times 10^{-4} \text{ s}^{-1}$) lasting for $\sim 7\text{h}$ each and having diameters of $\sim 5 \text{ Mm}$. Chian et al. (2020) observed that persistent vortices are formed in the gap regions of Lagrangian chaotic saddles at supergranular junctions with lifetimes varying from 28.5 to 298.3 min. In the same way, Roudier et al. (2021) (Figs. 16,17,18) detected vorticity resulting from the large horizontal velocity amplitude of a supergranule

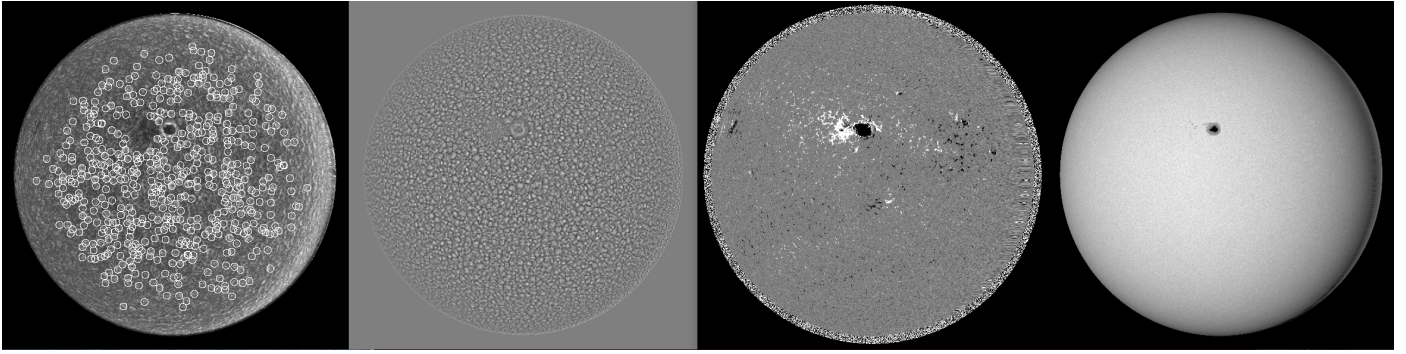


Fig. 14. Images of the Sun on 14 April 2016 showing spots and plages. From left to right: Velocity modulus u_h and the detected donuts (circles), divergence $\nabla \cdot \mathbf{u}_h$, longitudinal magnetic field, and continuum intensity.

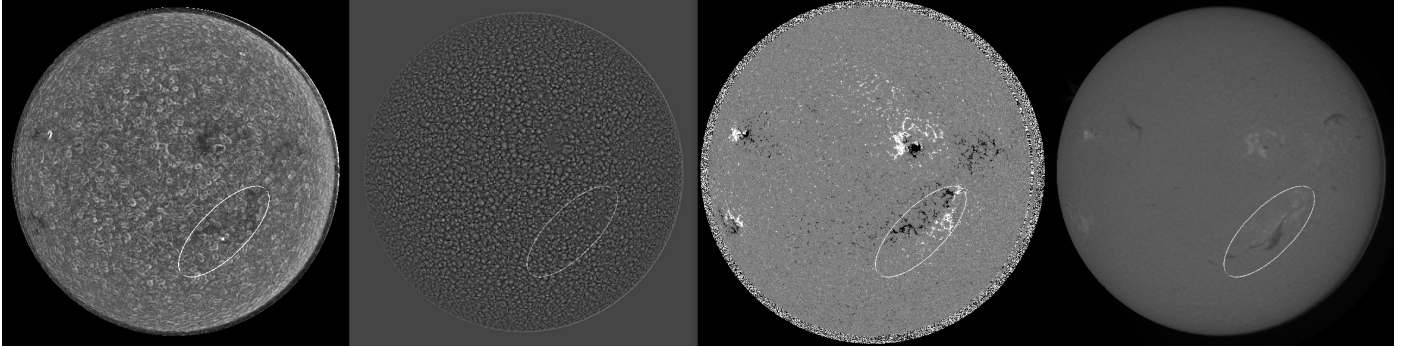


Fig. 15. Sunspot, plage, and filament on 26 January 2016. From left to right: Velocity modulus of u_h , divergence $\nabla \cdot \mathbf{u}_h$, longitudinal magnetic field, and $H\alpha$ observation (the ellipse indicates the filament region).

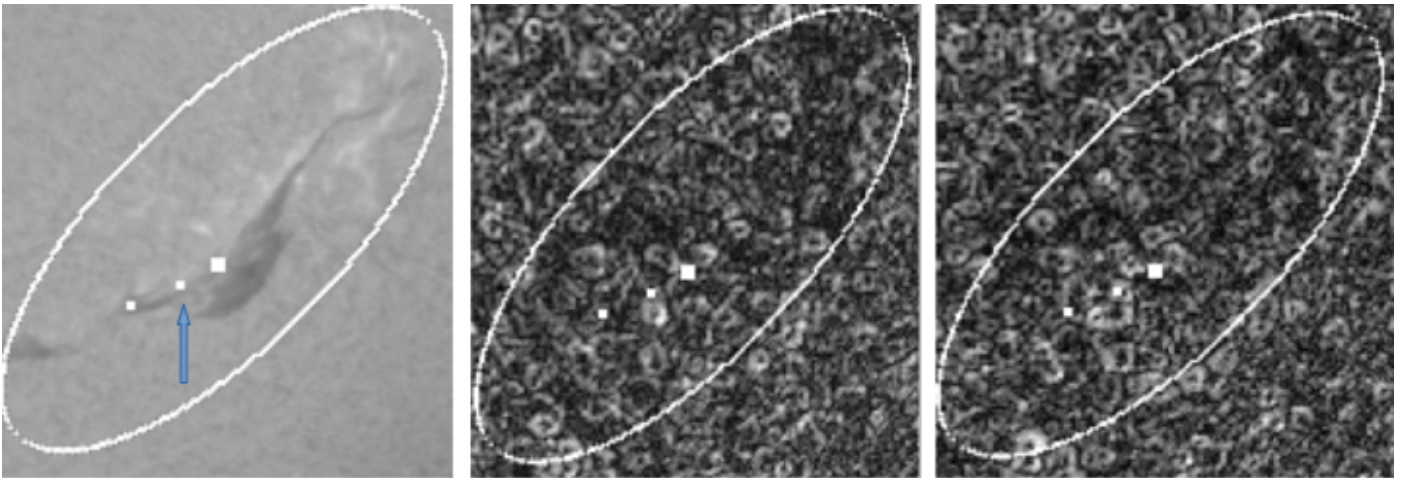


Fig. 16. Filament eruption in the $H\alpha$ line, on the left, on 26 January 2016 (16:30). The square, indicated by the arrow, indicates the foot where the eruption started at 17:00. The middle and right images represent the horizontal velocity modulus at time 12:00 and 16:00, respectively. For both images, intense donuts are observed close to 12:00 and at the location foot eruption at 16:00. The field of view is $561'' \times 572''$ ($401 \times 408 \text{ Mm}^2$)

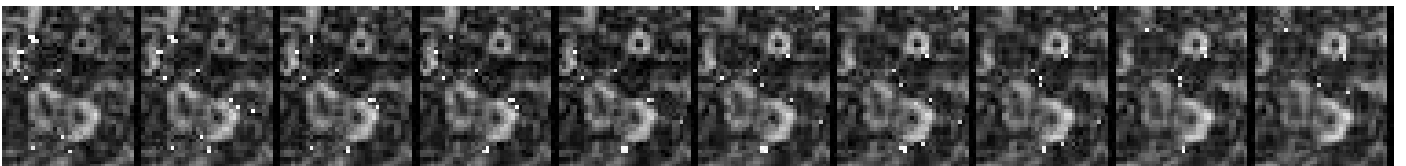


Fig. 17. Evolution of the velocity modulus u_h on 29 November 2018. The time step between each frame is 1 h and the field of view spans $127'' \times 155''$ ($90.9 \times 111 \text{ Mm}^2$). White squares indicate points where the vorticity modulus has an amplitude greater than $5.5 \times 10^{-5} \text{ s}^{-1}$.

with a donut shape and the combination of the velocities from the large neighboring supergranule.

These photospheric vortices are probably linked to the whirling motions discovered by Wedemeyer-Böhm et al. (2012) in the chromosphere, the atmospheric layer caught between the

photosphere and the corona. These structures are identified as observational signatures of rapidly rotating magnetic structures, which provide a mechanism for channeling energy from the lower into the upper solar atmosphere.

In addition to the vortex flow close to the supergranule, different phenomena (jet, blinkers, coronal bright points, etc.) are reported in the literature. Muglach (2021) describe coronal jets at the photospheric footpoints (Figs 1, 5 and 8) located at the supergranular boundaries with a convergence of the horizontal flows.

More recently, Panesar et al. (2021) have shown a link between small-scale transient brightenings (campfires) in the quiet Sun, which occur at the edges of photospheric magnetic network flux lanes, similarly to previous works (Porter et al. 1987; Porter & Dere 1991; Falconer et al. 1998; Gošić et al. 2014; Attie et al. 2016) in which active events are located at the boundaries of supergranule cells. In the same way, in Shokri et al. (2022) the small-scale brightenings in the transition region (blinkers) are observed at the boundaries of supergranules (see their Fig. 8).

All the phenomena presented here according to their description through the solar atmosphere are closely related to the supergranular flows and certainly the most powerful of them. As mentioned above, these observations are almost always related to very well-formed and generally clearly isotropic supergranular flows corresponding to the descriptions of our donuts. The detection of the donuts, and particularly the larger ones, could be a way to locate vortexes in the quiet Sun quickly.

For this purpose, we have tested the localization of vorticity from our surface velocities. From (u_θ, u_ϕ) , the vorticity fields have been computed with spatial (2.5 Mm) and temporal (30 minutes) steps, then averaged over 12 h with a running window. Figure 17 shows an example of the evolution of the large-amplitude vorticity region (greater than $5.5 \times 10^{-5} \text{ s}^{-1}$) plotted over the velocity modulus on 29 November 2018. In the bottom right of that figure, we observe long-lasting vorticity, around the large donuts, indicating a way to locate the important vortex on the solar surface. However, in order to be more conclusive, a larger sample size is needed to be statistically significant and also with the simultaneous localization of magnetic and vorticity phenomena in the whole solar atmosphere. These results indicate the potentiality of the vortex detection close to well-formed donuts.

7. Conclusion

On the Sun, the surface flows guide the evolution of the magnetic field elements at all scales of space and time. Supergranular diffusion and meridional flow advection of small-scale field elements play a role in the reversal of the global dipolar field.

In this study, we are interested in looking at the texture of the photospheric flows and the relation between the surface velocity amplitude and the photospheric magnetic field. The u_θ and u_ϕ horizontal flows on the solar surface issued from the CST allowed us to follow these flows on the whole surface of the Sun with very high spatial (2.5 Mm) and temporal resolution (30 minutes).

To characterize the kind of flow texture, the horizontal velocity modulus u_h has been studied. That quantity shows a different structuring from the divergence field issued from the same velocities, with different types of the spatial organization of the amplitude and shapes. In u_h maps, we observed closed annular flows, not necessarily joint, visible at all the latitudes which we referred to as donuts. However, the solar surface shows large areas without such elements with no structured flows, with a lower

amplitude. These donuts with an isotropic distribution of the velocity modulus reflect the most active convective cells associated with supergranulation. Our measurements show that the donuts have identical properties (amplitude, shape, orientation) regardless of their position on the Sun. Average donuts computed from all the donuts at the disk center ($\pm 10^\circ$) shows an east-west asymmetry in the amplitude which is related to previous works on the wave-like properties of supergranulation (Langfellner et al. 2018).

A kinematic simulation of the donuts' outflow represented by Gaussian sources, taking into account their locations, sizes, amplitudes, birth, and deaths, has been developed. That temporal simulated flows applied during 48h to passive particles (corks) show an empty area estimated to be 65% of the total area at the disk center which mimics the photospheric network. This indicates the preponderant action of the selected donuts which are, from our analysis, one of the major actors for the magnetic field diffusion on the quiet Sun.

Regarding the effect of the magnetic field on donuts formation, we observed the absence of donuts in the magnetized areas. In particular, the magnetic plages affect the strongest supergranular flows and thus this clearly modifies the diffusion of the magnetic field in these places. From filament destabilization observation, we noted horizontal flow activity via intense donuts close to the location of one filament foot where the eruption started. Such results must be confirmed with more statistical material.

One of the advantages of flow field measurement by the CST on long time series provided by SDO is the detection of the isotropic supergranules and all the physical events associated all over the solar surface. First, SDO data generalize the HINODE observations at the disk center to the whole surface of the Sun. The link between the families of granules and the isotropic horizontal flows (Roudier et al. 2016) indicates that TFGs work underneath in a continuous way and could be one of the main actors of the photospheric surface flows. That scenario has to be confirmed with more new observations.

More generally, the different phenomena observed in the solar atmosphere, such as blinkers, coronal bright points (campfires), or vortexes, are also closely related to the most powerful supergranular flows, which correspond to our donut. Then, the detection of donuts, especially the largest ones, could be an interesting way to locate and study the evolution of the magnetic network, the destruction of sunspots, the eruption of filaments, and also their influence on the upper layers via spicules, jets, and vortexes.

Acknowledgements. The HMI data is courtesy of the SDO HMI Science Investigation Team. Some of the computing was performed at the JSOC, which is located at the Stanford University and operated by the HMI Science Investigation Team. This work was granted access to the HPC resources of CALMIP under the allocation 2011-[P1115]. Thanks to C. Barnette for her contribution to the neural networks processing tests. We appreciate numerous team members who have contributed to the success of the SDO and Hinode mission. The MEDOC data and operations centre (CNES / CNRS / Univ. Paris-Saclay) make code availability and the CST documentation. These works are supported by COFFIES, NASA Grant 80NSSC20K0602. We thank the anonymous referee for her/his insightful comments, which have improved the paper.

References

- Attie, R., Innes, D. E., & Potts, H. E. 2009, A&A, 493, L13
- Attie, R., Innes, D. E., Solanki, S. K., & Glassmeier, K. H. 2016, A&A, 596, A15
- Berrilli, F., Del Moro, D., Consolini, G., et al. 2004, Sol. Phys., 221, 33
- Berrilli, F., Scardigli, S., & Del Moro, D. 2014, A&A, 568, A102
- Caroli, A., Giannattasio, F., Fanfoni, M., et al. 2015, Journal of Plasma Physics, 81, 495810514

- Chian, A. C. L., Silva, S. S. A., Rempel, E. L., et al. 2020, *Phys. Rev. E*, 102, 060201
- Cliver, E. W. & Knipp, D. J. 2021, *Astronomy and Geophysics*, 62, 6.38
- Del Moro, D., Berrilli, F., Duvall, T., & Kosovichev, A. G. 2004, *Solar Phys.*, 221, 23
- DeRosa, M. L. & Toomre, J. 2004, *ApJ*, 616, 1242
- Duvall, T. L. & Gizon, L. 2000, *Solar Phys.*, 192, 177
- Falconer, D. A., Moore, R. L., Porter, J. G., & Hathaway, D. H. 1998, *ApJ*, 501, 386
- Fan, Y. 2021, *Living Reviews in Solar Physics*, 18, 5
- Getling, A. V. & Kosovichev, A. G. 2022, arXiv e-prints, arXiv:2201.00638
- Giannattasio, F., Berrilli, F., Biferale, L., et al. 2014a, *A&A*, 569, A121
- Giannattasio, F., Berrilli, F., Consolini, G., et al. 2018, *A&A*, 611, A56
- Giannattasio, F., Stangalini, M., Berrilli, F., Del Moro, D., & Bellot Rubio, L. 2014b, *ApJ*, 788, 137
- Goldbaum, N., Rast, M. P., Ermolli, I., Sands, J. S., & Berrilli, F. 2009, *ApJ*, 707, 67
- Gošić, M., Bellot Rubio, L. R., del Toro Iniesta, J. C., Orozco Suárez, D., & Katsukawa, Y. 2016, *ApJ*, 820, 35
- Gošić, M., Bellot Rubio, L. R., Orozco Suárez, D., Katsukawa, Y., & del Toro Iniesta, J. C. 2014, *ApJ*, 797, 49
- Hirzberger, J., Gizon, L., Solanki, S. K., & Duvall, T. L. 2008, *Sol. Phys.*, 251, 417
- Langfellner, J., Birch, A. C., & Gizon, L. 2016, *A&A*, 596, A66
- Langfellner, J., Birch, A. C., & Gizon, L. 2018, *A&A*, 617, A97
- Langfellner, J., Gizon, L., & Birch, A. C. 2015a, *A&A*, 579, L7
- Langfellner, J., Gizon, L., & Birch, A. C. 2015b, *A&A*, 581, A67
- Meunier, N. & Roudier, T. 2007, *A&A*, 466, 691
- Meunier, N., Roudier, T., & Rieutord, M. 2008, *A&A*, 488, 1109
- Muglach, K. 2021, *ApJ*, 909, 133
- Orozco Suárez, D., Bellot Rubio, L. R., & Katsukawa, Y. 2012, in *Astronomical Society of the Pacific Conference Series*, Vol. 463, Second ATST-EAST Meeting: Magnetic Fields from the Photosphere to the Corona., ed. T. R. Rimmele, A. Tritschler, F. Wöger, M. Collados Vera, H. Socas-Navarro, R. Schlichenmaier, M. Carlsson, T. Berger, A. Cadavid, P. R. Gilbert, P. R. Goode, & M. Knölker, 57
- Panesar, N. K., Tiwari, S. K., Berghmans, D., et al. 2021, *ApJ*, 921, L20
- Porter, J. G. & Dere, K. P. 1991, *ApJ*, 370, 775
- Porter, J. G., Moore, R. L., Reichmann, E. J., Engvold, O., & Harvey, K. L. 1987, *ApJ*, 323, 380
- Requerey, I. S., Cobo, B. R., Gošić, M., & Bellot Rubio, L. R. 2018, *A&A*, 610, A84
- Rieutord, M., Meunier, N., Roudier, T., et al. 2008, *A&A*, 479, L17
- Rincon, F. & Rieutord, M. 2018, *Living Reviews in Solar Physics*, 15, 6
- Rincon, F., Roudier, T., Schekochihin, A. A., & Rieutord, M. 2017, *A&A*, 599, A69
- Roudier, T., Malherbe, J. M., Gelly, B., et al. 2020, *A&A*, 641, A50
- Roudier, T., Malherbe, J. M., Rieutord, M., & Frank, Z. 2016, *A&A*, 590, A121
- Roudier, T., Rieutord, M., Brito, D., et al. 2009, *A&A*, 495, 945
- Roudier, T., Rieutord, M., Malherbe, J. M., et al. 2012, *A&A*, 540, A88
- Roudier, T., Rieutord, M., Prat, V., et al. 2013, *A&A*, 552, A113
- Roudier, T., Schmieder, B., Filippov, B., Chandra, R., & Malherbe, J. M. 2018a, *A&A*, 618, A43
- Roudier, T., Švanda, M., Ballot, J., Malherbe, J. M., & Rieutord, M. 2018b, *A&A*, 611, A92
- Roudier, T., Švanda, M., Malherbe, J. M., et al. 2021, *A&A*, 647, A178
- Scherrer, P. H., Schou, J., Bush, R. I., et al. 2012, *Sol. Phys.*, 275, 207
- Schou, J., Scherrer, P. H., Bush, R. I., et al. 2012, *Sol. Phys.*, 275, 229
- Shine, R., Simon, G., & Hurlburt, N. 1999, in *SOHO-9 Workshop on Helioseismic Diagnostics of Solar Convection and Activity*, Vol. 9, 15
- Shokri, Z., Alipour, N., Safari, H., et al. 2022, *ApJ*, 926, 42
- Simon, G. & Leighton, R. 1964, *ApJ*, 140, 1120
- Simon, G., Title, A., & Weiss, N. 1991, *ApJ*, 375, 775
- Simon, G. W. & Weiss, N. O. 1989, *ApJ*, 345, 1060
- Srikanth, R., Singh, J., & Raju, K. P. 2000, *ApJ*, 534, 1008
- Title, A. M., Tarbell, T. D., Topka, K. P., et al. 1989, *ApJ*, 336, 475
- Title, A. M., Topka, K. P., Tarbell, T. D., et al. 1992, *ApJ*, 393, 782
- Švanda, M., Roudier, T., Rieutord, M., Burston, R., & Gizon, L. 2013, *ApJ*, 771, 32
- Švanda, M. 2013, *Central European Astrophysical Bulletin*, 37, 447
- Wang, Y. M., Warren, H. P., & Muglach, K. 2016, *ApJ*, 818, 203
- Wedemeyer-Böhm, S., Scullion, E., Steiner, O., et al. 2012, *Nature*, 486, 505
- Williams, P. E., Pesnell, W. D., Beck, J. G., & Lee, S. 2014, *Sol. Phys.*, 289, 11
- Wollmann, J., Švanda, M., Korda, D., & Roudier, T. 2020, *A&A*, 636, A102

Appendix A: Movies

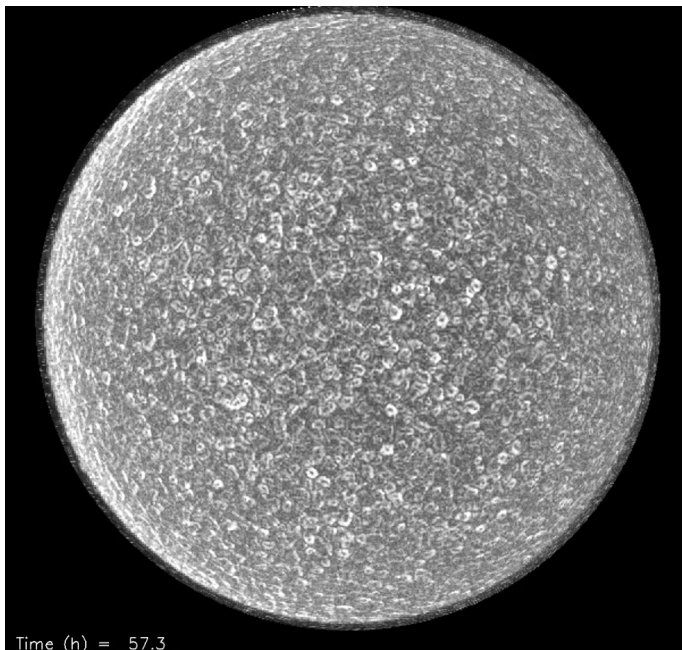


Fig. A.1. (online movie) Photospheric horizontal velocity modulus during 6 days, derotated from the solar differential rotation. A smoothing window of 12h was applied to reduce the noise. The reference day, center of the Sun, and solar radius for CST code were taken at 00:00 UTC of the fourth observation day, that is 29 November 2018.

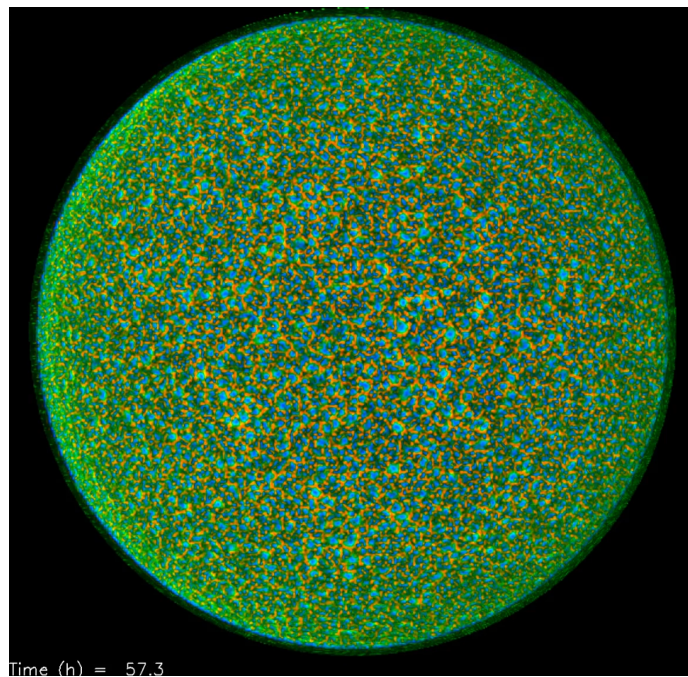


Fig. A.3. (online movie) Combination of movie 1's horizontal velocity modulus and that of movie 2. The horizontal velocity modulus was coded in white between 0 and 0.75 km/s, and the divergence in red (convergence between 0 and $-1 \times 10^{-5} \text{s}^{-1}$) and blue (divergence between 0 and $+1 \times 10^{-5} \text{s}^{-1}$). We observed the maximum velocities surrounding the diverging areas.

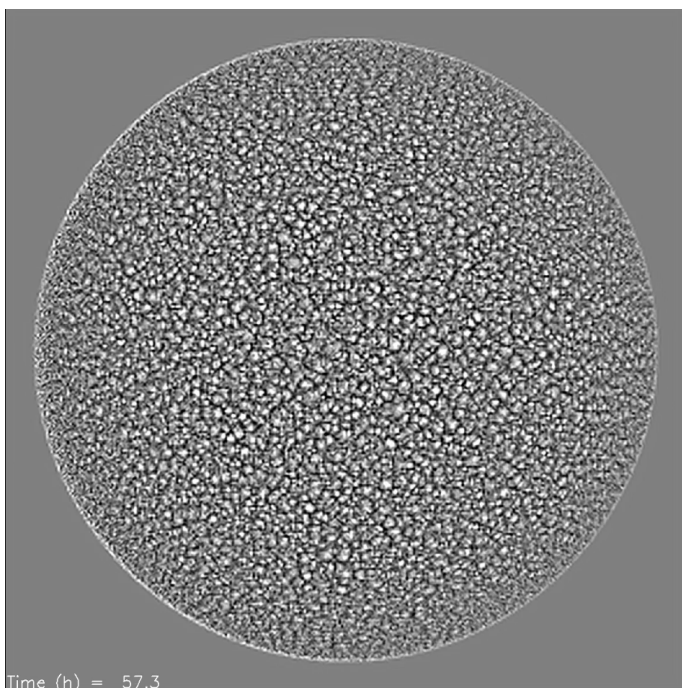


Fig. A.2. (online movie) Divergence field computed from the horizontal velocity during 6 days, derotated from the solar differential rotation. A smoothing window of 12h was applied to reduce the noise. The reference day, center of the Sun, and solar radius for CST code were taken at 00:00 UTC of the fourth observation day, that is 29 November 2018.